

# A Deep Learning Approach to Teeth Segmentation and Orientation from Panoramic X-rays

Mrinal Kanti Dhar<sup>1,\*,#</sup>, Mou Deb<sup>2,#</sup>, D. Madhab<sup>3</sup>, and Zeyun Yu<sup>4</sup>

<sup>1</sup>Leading University, Bangladesh

<sup>2</sup>South Dakota School of Mines and Technology, USA

<sup>3</sup>Shaparan Govt. College, Bangladesh

<sup>4</sup>SprintRay Inc., USA

\*Corresponding author: [mrinal054@lus.ac.bd](mailto:mrinal054@lus.ac.bd)

#Authors have equal contributions.

**Abstract** – Accurate teeth segmentation and orientation are fundamental in modern oral healthcare, enabling precise diagnosis, treatment planning, and dental implant design. In this study, we present a comprehensive approach to teeth segmentation and orientation from panoramic X-ray images, leveraging deep learning techniques. We build our model based on FUSegNet, a popular model originally developed for wound segmentation, and introduce modifications by incorporating grid-based attention gates into the skip connections. We introduce oriented bounding box (OBB) generation through principal component analysis (PCA) for precise tooth orientation estimation. Evaluating our approach on the publicly available DNS dataset, comprising 543 panoramic X-ray images, we achieve the highest Intersection-over-Union (IoU) score of 82.43% and Dice Similarity Coefficient (DSC) score of 90.37% among compared models in teeth instance segmentation. In OBB analysis, we obtain the Rotated IoU (RIoU) score of 82.82%. We also conduct detailed analyses of individual tooth labels and categorical performance, shedding light on strengths and weaknesses. The proposed model’s accuracy and versatility offer promising prospects for improving dental diagnoses, treatment planning, and personalized healthcare in the oral domain. Our generated OBB coordinates and codes are available at [https://github.com/mrinal054/Instance\\_teeth\\_segmentation](https://github.com/mrinal054/Instance_teeth_segmentation).

**Keywords** – instance teeth segmentation, panoramic X-ray images, oriented bounding boxes (OBB), FUSegNet, PCA.

## 1 Introduction

Accurate teeth segmentation is important in oral healthcare. It provides location data for orthodontic treatments, clinical diagnoses, and surgical procedures. It is also used to identify individuals, capture tooth morphology, and plan dental implants [1]. Manually segmenting teeth is time-consuming and challenging, even for experienced professionals. Semi-automatic techniques can help, but they still require some human input. This is especially true for lower-resolution images, where it can be difficult to accurately delineate certain tooth regions.

Teeth segmentation from panoramic X-ray images can be of two types – semantic segmentation and instance segmentation. Semantic segmentation is a simple approach to dental analysis that labels the entire teeth region with a single label. This simplicity makes it computationally efficient and easier to implement. Semantic segmentation is well-

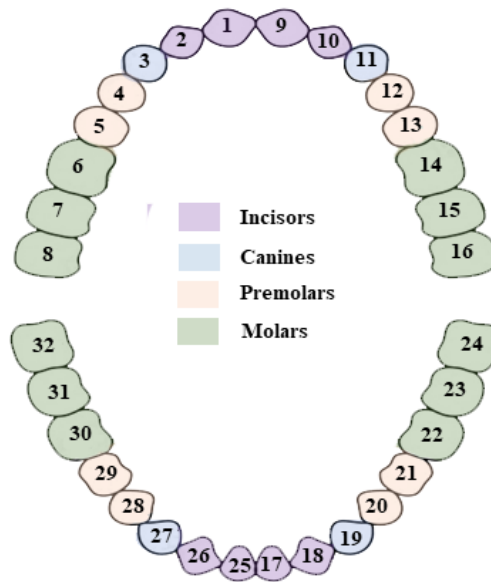


**Figure 1** Teeth labeling used in this paper. Each tooth is assigned a label from 1 to 32. Additionally, teeth are categorized into four groups: incisors, canines, premolars, and molars, with each group having upper and lower versions

suited for general dental analysis where distinguishing individual teeth is not essential, such as identifying overall dental health or disease patterns. Semantic segmentation could be used to track the progression of dental diseases over time. This would allow dentists to monitor the effectiveness of treatment and make adjustments as needed. Teeth instance segmentation assigns separate labels to each individual tooth, enabling precise identification of each tooth's boundaries and characteristics. With instance segmentation, dental professionals can accurately analyze the health of each tooth, aiding in personalized treatment planning for orthodontic procedures and other dental interventions. A dentist can use instance segmentation to identify a tooth that is decayed. This information can be used to plan the best course of treatment, such as a filling or a root canal. Instance segmentation allows for detailed quantitative analysis, such as measuring gaps between teeth, assessing wear patterns, and monitoring specific dental issues on a per-tooth basis. For tasks like designing dental prosthetics or implants, instance segmentation helps in creating accurate models that fit each tooth precisely.

While 3D instance segmentation is particularly valuable for complex cases that require a thorough understanding of tooth morphology, such as orthognathic surgery planning, dental implant placement, and in-depth orthodontic assessments, 2D instance segmentation is well-suited for routine dental analyses and treatments that can be effectively assessed from a two-dimensional perspective, such as cavity detection, treatment planning, and basic orthodontic evaluations. 2D instance segmentation is generally faster and requires less computational resources compared to its 3D counterpart, making it suitable for tasks that demand quick results.

In this paper, we use panoramic dental X-ray images for instance segmentation. Panoramic X-ray images are widely used for applications like dental caries, alveolar bone resorption, and impacted teeth [2]. Research works on panoramic X-ray images are mostly limited to teeth detection, teeth segmentation, and teeth numbering. Orientations of teeth are

not well explored. It can help dentists and oral surgeons diagnose dental problems and plan treatments, particularly for procedures related to restorative dentistry, such as dental implants, teeth alignment, and orthodontic interventions. Typically, positioning technology and segmentation are conducted in separate frameworks. Consequently, the development cycle takes longer, and the algorithm's complexity is elevated [3].

Our contribution to this paper can be summarized as –

- We propose a two-stage framework that returns individual segmented teeth and their orientations. We adopt a deep learning-based approach to segment individual teeth, followed by applying Principal Component Analysis (PCA) to determine tooth orientation. Such outcomes can facilitate obtaining precise teeth positions in an image.
- We modify the FUSegNet model [4], originally developed for wound segmentation, for teeth instance segmentation by introducing grid-based attention gates in skip connections.
- We extend our approach to find horizontal bounding boxes (HBB), oriented bounding boxes (OBB), and missing teeth detection.
- We generate the OBB coordinates for each of the teeth in the DNS dataset [5], and these coordinates are available in our GitHub repository.
- We provide comprehensive experimental findings, including a comparison with the state-of-the-art, and an in-depth examination of our technique with a comprehensive ablation study to show the efficacy of our approach.

## 2 Literature Review

Deep learning can help dentists by automating the process of teeth segmentation. This saves time and reduces human error, allowing dentists to focus on more important tasks such as accurate diagnosis and treatment planning. Various methods have been developed for teeth segmentation. Koch et al. [6] employed FCN in a U-Net setup. Zhao et al. [7] introduced TSASNet with a two-stage approach involving contextual attention and segmentation based on attention maps. Chen et al. [8] extended spatial pyramid pooling (SPP) to MSLPNet and introduced MS-SSIM loss. Salih and Kevin [9] proposed LTPEDN, replacing LBC layers with LTP layers. Hou et al. [10] proposed Teeth U-Net using a multi-scale feature aggregation attention block (MAB) and dilated hybrid self-attention block (DHAB) in the bottleneck layer for improved segmentation.

Jader et al. [11] are credited for being the pioneers who attempted teeth instance segmentation from panoramic X-ray images. They employed a set of 193 images for training and subsequently assessed their approach on 1224 images, achieving an F1-score of 88%. Rubiu et al. [12] also used Mask R-CNN on Tufts Dental Database [13] which consists of 1000 panoramic dental radiographs including both deciduous and permanent teeth. Their classification accuracy and dice score were 98.4% and 87%, respectively, and observed poor segmentation for the right mandibular third molar. Silva et al. [5] explored Mask R-CNN, PANet, HTC, and ResNeSt for teeth segmentation and numbering. They observed the best result for PANet with 71.3% of mAP for segmentation. Helli and Mahamci [14] employed a two-step methodology where they employed a U-Net to create binary prediction followed by morphological operations to label

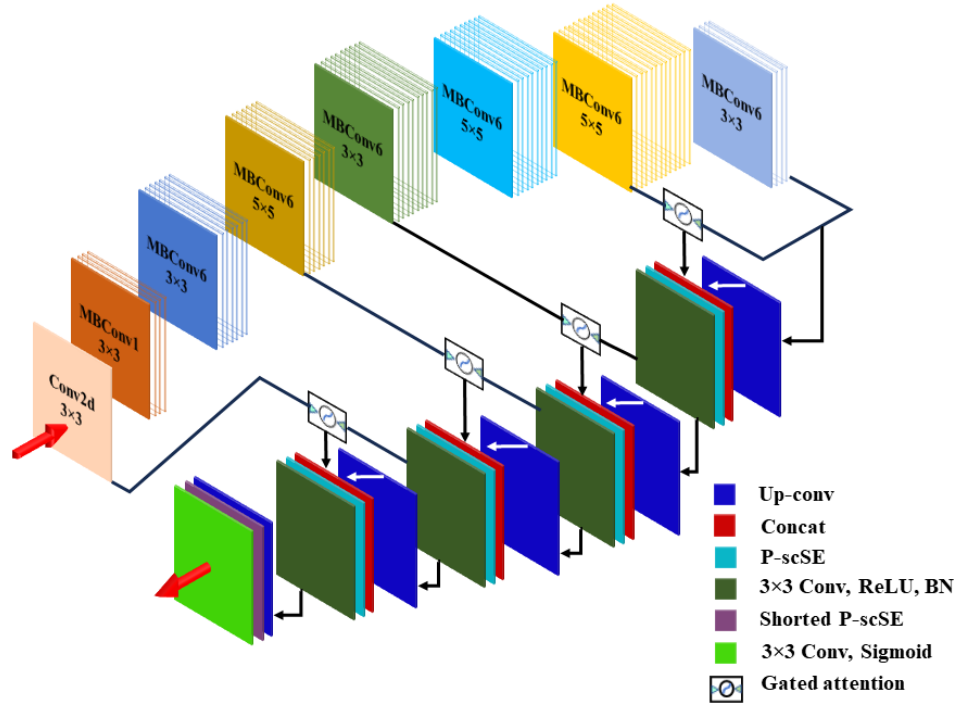


**Figure 2** Proposed model. It is a modified version of FUSegNet. An attention gate is introduced to the skip-connections of FUSegNet.

connecting elements. So, the full segmentation process is not deep learning-based. Their study utilized a limited dataset comprising 116 patients, with 11 images reserved for testing purposes. El Bsat et al. [15] tried MobileNet, AdapNet, DenseNet, and SegNet for maxillary teeth and palatal rugae segmentation. Their dataset consists of 797 occlusal views from teeth photographs. They achieved the best performance from SegNet with 86.66% average mIoU.

The above-mentioned works primarily addressed teeth segmentation, with some including numbering, yet none tackled tooth orientation. However, the orientation of teeth in 2D panoramic X-ray images is significant because it can help dentists identify the position of the teeth and their roots. This paper presents a two-stage framework: initially, utilizing deep learning for precise teeth segmentation, enabling subsequent numbering based on individual labels; subsequently, employing principal component analysis (PCA) [16] to establish tooth orientation.

### 3 Materials and Methods

#### 3.1 Dataset

In this paper, we use the publicly available DNS dataset, which is accessible upon request to the authors of [5]. The dataset contains 543 panoramic X-ray images, each with a resolution of 1991 by 1127 pixels. Among them, 324 images are kept for training, 108 for validation, and 111 for inference. To fit the images on the GPU, we create small patches with a size of  $512 \times 512$  pixels. Adjacent patches have a  $10 \times 10$  overlap as the patch window slides, and all images are normalized between 0 and 1. In addition, for training the deep learning models, a unique segmentation label is assigned to each tooth, resulting in a total of 32 segmentation labels. The distribution of segmentation labels is depicted in Figure 1. Furthermore, we create oriented bounding box coordinates for each tooth using a PCA-based approach.

### 3.2 Model Architecture

Figure 2 demonstrates our deep learning model. We modify the FUSegNet model and introduce grid-based attention gates in the skip connections of the FUSegNet. It has four major parts – encoder, decoder, grid-based attention gates (AG), and parallel spatial and channel squeeze-and-excitation (P-scSE) module.

#### 3.2.1 Encoder

To avoid manual scale adjustments, the study employs an EfficientNet architecture as the core encoder. Convolutional neural networks often require tweaking depth, width, and resolution, a traditionally cumbersome and random process. EfficientNet’s authors [17] introduce a novel approach, using fixed coefficients ( $\alpha$ ,  $\beta$ , and  $\gamma$ ) and a compound coefficient  $\phi$  for uniform scaling. Depth, width, and resolution are scaled as  $\alpha^\phi$ ,  $\beta^\phi$ , and  $\gamma^\phi$ , respectively. The authors used neural architecture search (NAS) to set EfficientNet-B0’s  $\alpha$ ,  $\beta$ , and  $\gamma$  at 1.2, 1.1, and 1.15, respectively. After a small grid search (constraint  $\alpha \cdot \beta^2 \cdot \gamma^2 \approx 2$ ),  $\phi$  variations led to EfficientNet-B1 to B7. While EfficientNet-B0 is  $224 \times 224$ , EfficientNet-B7 has  $\phi=6$ , yielding  $224 \times \gamma^\phi = 224 \times 1.15^6 \approx 518$  resolution. So, we use an EfficientNet-B7 model trained on ImageNet for patches of size  $512 \times 512$ .

#### 3.2.2 Decoder

As depicted in Figure 2, during each decoder stage, the upsampled output from the lower level is first concatenated with the encoder output of the corresponding level. However, in contrast to the FUSegNet architecture, the encoder output undergoes processing through a grid-based gated attention module [18]. This is done to regulate the flow along the skip connections and allow the attention coefficients to focus more specifically on local regions. The resulting concatenated output then passes through the P-scSE attention module, which aggregates spatial and channel-wise information. Finally, a  $3 \times 3$  Convolution-ReLU-Batch normalization is applied to this output.

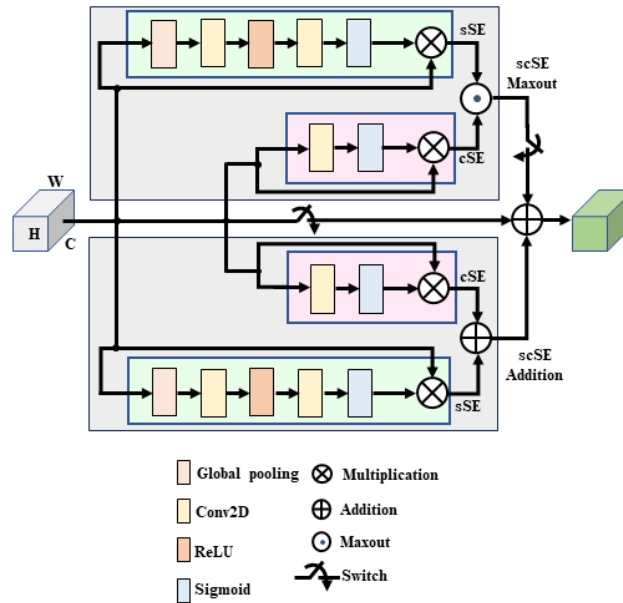
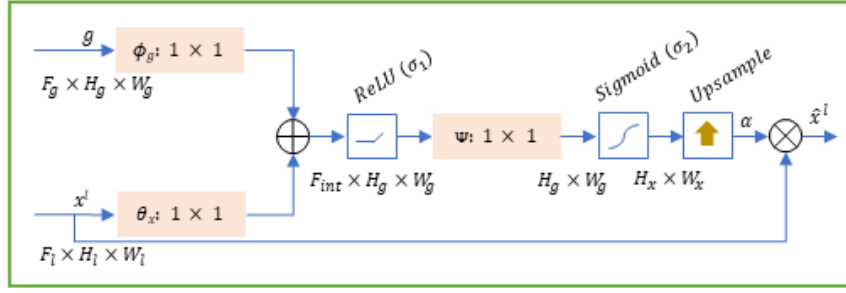


Figure 3 Architecture of parallel scSE (P-scSE)



**Figure 4** Grid-based attention gate. The figure is taken from [31].

### 3.2.3 Parallel spatial and channel squeeze-and-excitation (P-scSE)

The squeeze-and-excitation module [19] was designed to boost the network's representational power by highlighting significant features and ignoring less relevant ones. It generates a channel descriptor using global average pooling, triggering channel-related dependencies. It is also referred to as cSE due to its channel-wise excitation. Roy et al. [20] introduced the sSE module, which squeezes along the channel axis and excites along spatial dimensions. The scSE module combines the cSE and sSE components. This combination can be done in different ways. As shown in Figure 3, P-scSE [4] creates two parallel branches of the scSE module – one by adding cSE and sSE, and the other by taking the maximum of them. While max-out offers competitiveness between the channel and spatial excitations, addition aggregates these two excitations. A switch is provided to skip max-out when the number of channels is small. When we have a small number of channels, the model's capacity to learn intricate channel dependencies and patterns is already limited. So, if we selectively collect features, like max-out does, it will lose some important features and will not contribute significantly.

### 3.2.4 Grid-based attention gate

In this paper, we use grid-based attention gates (AG) [18] to improve skip connections. The AG is a trainable module that is added to skip connections of encoder-decoder-based architecture to the number of false positive predictions for small objects with significant shape variation. It learns to weigh the features from the skip connections, giving more importance to the features that are relevant to the target structure. As shown in Figure 4, the attention gate calculates the attention coefficient  $\alpha$ , which is the result of additive attention computed from the input feature maps  $x$  and contextual information provided by the gating signal  $g$ . The attention coefficient identifies important spatial regions by paying attention to task-relevant activations.

## 3.3 Post-processing

The output of the deep learning model is fine-tuned by implementing a post-processing stage. If two regions with the same label exist, the larger region is identified as the desired region, while the smaller region is categorized as unwanted. Initially, we identify border pixels using chain coding. Subsequently, we detect neighboring pixels of each border pixel using 8-connectivity. We only consider those neighboring pixels with intensities differing from those of the unwanted portion. As shown in Figure 5, we observe three cases that need to be taken care of.

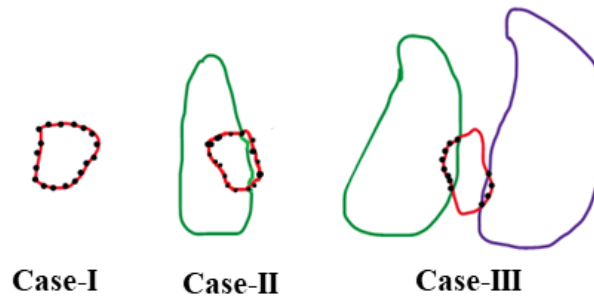


**Figure 5** Three cases observed in the segmentation results. Red color indicates the unwanted regions. Black dots indicates border pixels. If two regions share the same label, then the larger one is identified as the desired region, and the smaller one is categorized as unwanted

*Case-I:* If all the neighbor pixels are 0 (background), then dissolve the unwanted portion into the background.

*Case-II:* If the neighbor pixels consist of background pixels and pixels of a specific label, then –

- First, ignore background pixels.
- Then, dissolve the unwanted portion into label pixels.

*Case-III:* If there exist two different labels in the neighbor pixels, then –

- Count the number of border pixels that lie in both labels
- The most frequent label is the winner

### 3.4 Oriented Bounding Box (OBB)

To implement the oriented bounding box (OBB), we utilize principal component analysis (PCA) [16]. PCA is a statistical technique that transforms correlated observations into uncorrelated values called principal components. It ensures the first component captures the most variance, and subsequent components maximize variance while staying uncorrelated with preceding ones through orthogonal transformations. The steps involved in generating OBBs in this paper are as follows –

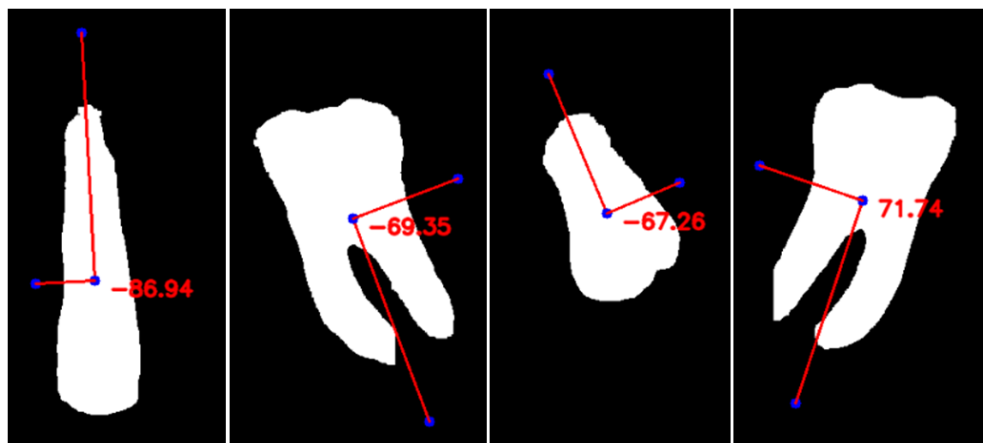


**Figure 6** Examples of  $PCA_{Angle}$ . Angles are shown for PC1 w.r.t. the horizontal axis.



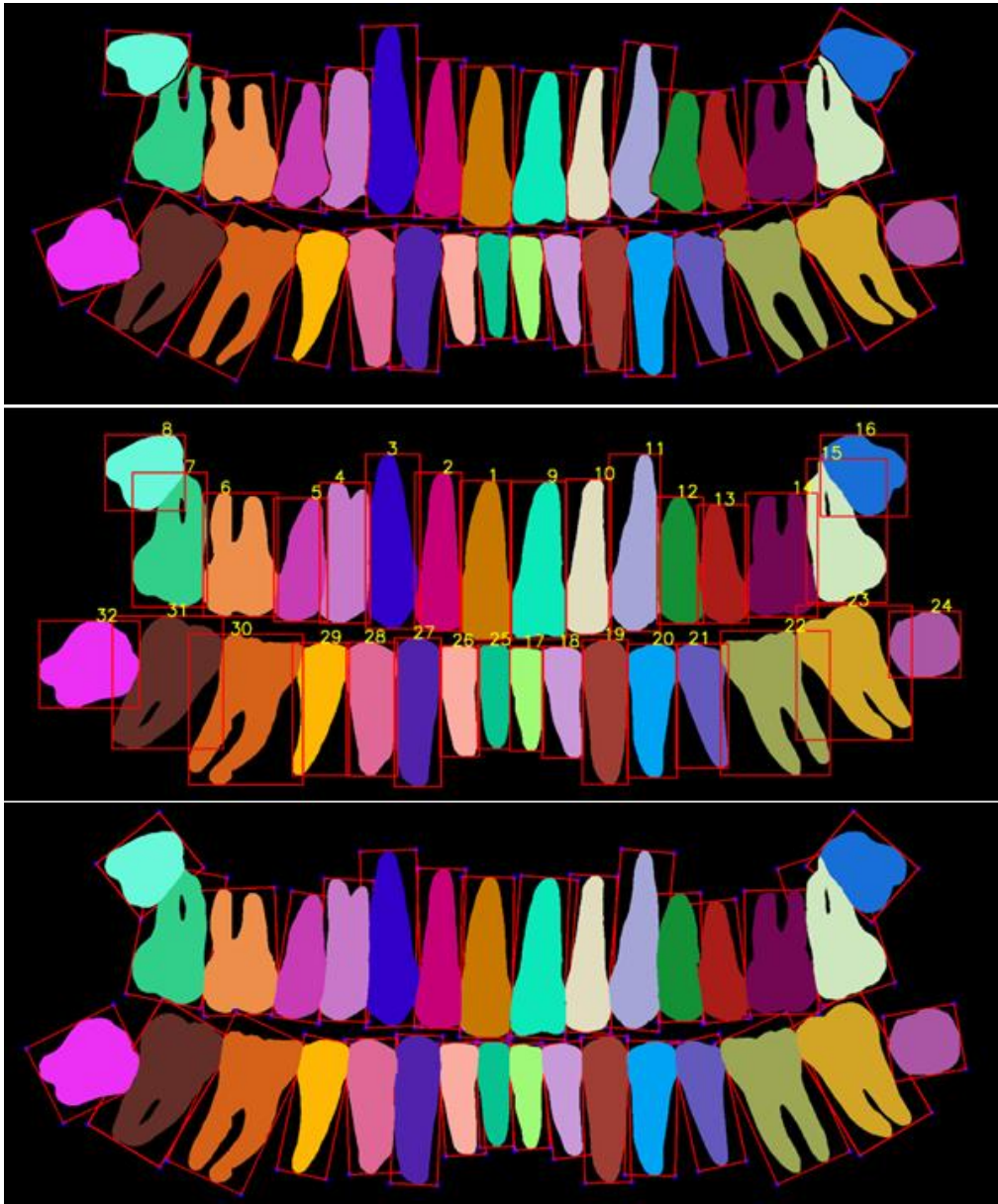


**Figure 7** Segmentation results. (top) Ground truth, (middle) Segmentation results with HBB, and (bottom) Segmentation results with OBB.

*Tooth separation:* We approach the OBB generation for each tooth individually. This involves keeping one tooth in the image while rendering the others as background. The image is then binarized.

*PCA:* We then calculate the first two major principal components (PCs) and determine the angle between the first PC and the horizontal axis, which we refer to as  $PCA_{angle}$ .

*Rotation:* We then generate a 2D rotation matrix to rotate the tooth and align it vertically. The rotation matrix for rotating a point  $(x, y)$  by an angle,  $\theta$  around an arbitrary pivot  $(x_c, y_c)$  can be expressed as –

$$\begin{bmatrix} x' \\ y' \\ 1 \end{bmatrix} = \begin{bmatrix} \cos \theta & -\sin \theta & x_c(1 - \cos \theta) + y_c \sin \theta \\ \sin \theta & \cos \theta & y_c(1 - \cos \theta) - x_c \sin \theta \\ 0 & 0 & 1 \end{bmatrix} \begin{bmatrix} x \\ y \\ 1 \end{bmatrix} \quad (1)$$



We calculate  $\theta$  in the following way –

$$\begin{cases} \theta = 180 + (90 - PCA_{angle}) & \text{if } PCA_{angle} < 0 \\ \theta = (90 - PCA_{angle}) & \text{otherwise} \end{cases} \quad (2)$$

*HBB*: After aligning the tooth vertically, we proceed to plot the horizontal bounding box (HBB). Generating an HBB from contour points is much easier than generating an OBB.

*Inverse rotation*: We then rotate the tooth along with the HBB back to its original position. To achieve this, we substitute  $(-\theta)$  into equation (1).

### 3.5 Training and Evaluation

*Experimental setup*: All experiments are executed on Google Colab Pro+. For optimization, we use Adam optimizer [21] with an initial learning rate of 0.001 and weight decay of 1e-5. The learning rate is decreased by a factor of 0.1 when the metric shows no improvement for 10 epochs. Models are trained for 50 epochs and the best model is stored. We employ a combined loss function, using both dice loss and focal loss with equal weights. Unlike cross-entropy loss, which overlooks contextual information of surrounding pixels in favor of per-pixel calculation, dice loss accounts for local and global information. Dice loss, represented as  $DL = (1 - DSC)$ , encompasses the dice coefficient ( $DSC$ ). Focal loss ( $FL$ ) is valuable for addressing class imbalance (such as background  $\gg$  foreground), where it prioritizes challenging cases by down-weighting easy examples [22]. So, the final loss function is expressed as –

$$\mathcal{L} = DL + FL \quad (3)$$

*Evaluation metric*: For the segmentation task, we use intersection-over-union (IoU), precision, recall, and dice score (DSC). For encoder-decoder-based architecture, these evaluation metrics are widely used. Here are each definition's details –

$$Precision = \frac{TP}{TP+FP} \quad (4)$$

$$Recall = \frac{TP}{TP+FN} \quad (5)$$

$$DSC = \frac{2TP}{2TP+FP+FN} \quad (6)$$

$$IoU = \frac{TP}{TP+FP+FN} \quad (7)$$

Here, TP, FP, and FN are true positive, false positive, and false negative, respectively.

For OBB, we calculate IoU between the ground truth OBB and predicted OBB. In later sections, it will be termed as rotated IoU (RIoU) to distinguish it from the IoU used in segmentation.

## 4 Results and Discussion

We can divide our experiments into two parts: segmentation analysis and OBB analysis. In segmentation analysis, we compare our proposed model with state-of-the-art segmentation models. Since our goal is to develop an encoder-decoder-based architecture, we primarily compare the results with popular encoder-decoder structures. We tabulate the results in Table 1. As shown in the table, our proposed model achieves an IoU score of 82.43% and a DSC score of 90.37%, both of which are the highest scores compared to the other models. Additionally, it is evident that the proposed modification to the original FUSegNet model yields slightly better results. We also explore two transformer-based approaches. The first one is MiT-b2 UNet, where we incorporate the SegFormer (b2-sized) encoder [32] pretrained on ImageNet with the UNet architecture. The second one is Swin-Unet [33]. However, we do not observe satisfactory performance with transformer-based approaches. Possibly it is because transformers often tend to overfit for small-scale data due to the lack of structural bias [34] or require additional task-specific tuning [35].

**Table 1** Segmentation results achieved from deep learning models

Model	IoU	Precision	Recall	DSC
DeepLabV3+ [25]	80.45	88.59	89.75	89.17
FPN [26]	81.75	89.54	<b>90.28</b>	89.76
MANet [27]	62.70	85.82	69.95	77.08
LinkNet [28]	35.25	73.63	40.35	52.13
FUSegNet [4]	80.79	88.51	90.26	89.38
PSPNet [29]	28.94	59.60	36.00	44.89
UNet [30]	67.93	86.00	76.37	80.90
MiT-b2 UNet [32]	72.65	86.80	81.67	84.16
Swin-Unet [33]	53.69	72.43	67.47	69.87
<b>Ours</b>	<b>82.43</b>	<b>90.48</b>	90.26	<b>90.37</b>

**Table 2** Rotated IoU (RIoU), false positives (FP), and false negatives (FN) calculated from OBBs achieved by our proposed method.

RIoU	FP	FN
82.82	0	3~6

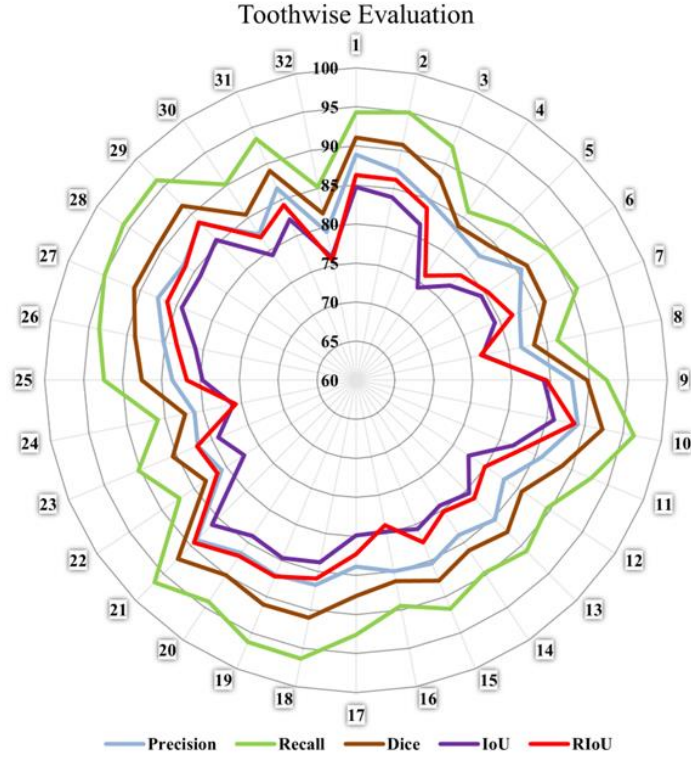


**Figure 8** Radar diagram to demonstrate toothwise evaluation.

For OBB performance analysis, we first generate oriented bounding boxes using the method described earlier and calculate rotated IoU (RIoU). We prefer IoU over mean average precision because, unlike other region proposal-based detection methods, oriented bounding boxes generated from encoder-decoder-based approaches do not have any confidence scores. Figure 6 illustrates the  $PCA_{angle}$  of some example teeth, which is subsequently used to calculate the tooth rotation angle,  $\theta$ . As shown in Table 2, we achieve an RIoU score of 82.82%. Figure 7 illustrates segmentation performance through the visualization of predictions compared to the ground truth, and it also presents the segmentation results using both horizontal bounding boxes and oriented bounding boxes.

So far, the evaluation is based on the entire dataset. We calculate the mean evaluation matrices for each individual tooth label in the entire dataset. However, this approach sometimes does not accurately reflect the performance of individual tooth labels. Therefore, we need to evaluate the 32 individual tooth labels separately. As shown in Figure 8, we generate a radar chart to demonstrate the performance of each label. We observe that tooth labels 4, 8, 22, 24, and 32 show relatively poor performance compared to the other labels in terms of DSC and RIoU. Their DSC scores range from 80% to 85%, and their RIoU ranges from 75% to 80%. In contrast, tooth labels 1-2, 9-10, 18-19, 20-21, and 27-29 demonstrate relatively high performance with DSC scores ranging from 90% to 95% and RIoU ranging from 85% to 90%.

**Table 3** Categorical evaluation of teeth.

Label	Precision	Recall	DSC	IoU	RIoU
Upper incisors	88.25	94.45	90.95	84.66	86.39
Lower incisors	84.84	93.76	88.77	81.11	83.35
Upper canine	85.31	92.54	88.36	81.73	83.47
Lower canine	87.27	95.64	90.96	84.44	86.74
Upper premolars	83.43	88.58	85.29	77.30	79.09
Lower premolars	87.65	95.69	91.19	84.90	87.84
Upper molars	84.04	89.67	86.05	79.19	80.08
Lower molars	82.10	88.81	84.61	78.42	80.28

Next, we perform categorical analysis. As shown in Figure 1, 32 teeth are divided into 4 categories – incisors, canines, premolars, and molars. Each of these categories is further divided into two groups – upper and lower. So, in total, we have 8 categories. Categorical analysis is presented in Table 3. It is observed that incisors and canines, for both upper and lower jaws, demonstrate good performance. Lower premolars also exhibit good performance. These five categories achieve a DSC of  $>88\%$  and an RIoU of  $>83\%$ . However, upper premolars, along with both upper and lower molars, show relatively poor performance, with a DSC of  $\leq 86\%$  and an RIoU of  $\leq 80\%$ .

We identify several factors that influence the model’s performance. Lack of instance overlapping, presence of foreign bodies, fuzzy tooth roots, and poor annotations are some of the factors that affect the performance. As shown in Figure 9(a-b), there are overlaps between premolar teeth and between premolar and molar teeth in the panoramic X-ray images; however, there is no instance overlapping in the ground truths. Foreign bodies include dental restorations, broken dental instruments, metal fillings, bracelets, and other metal objects. Figure 9(c) shows the presence of bracelets and fillings, while Figure 9(d) shows the presence of fuzzy tooth roots. As shown in Figure 9(e), some images are poorly annotated and contain sharp edges and cones. However, when compared to the original data, our model predicts smoother edges, which is more reasonable. While some researchers have made modifications to improve the dataset’s quality [23][24], in this work, we have used the original dataset as it is publicly available.

Furthermore, we calculate the number of false positives and false negatives in OBBs. This is performed to detect missing teeth. There are a total of 3,382 teeth in the 111 test images. We train and evaluate our model 5 times. As shown in Table 2, we do not observe any false positives in any of the runs, and the number of false negatives ranges from 3 to 6. This indicates that the model can be used effectively for detecting missing teeth.

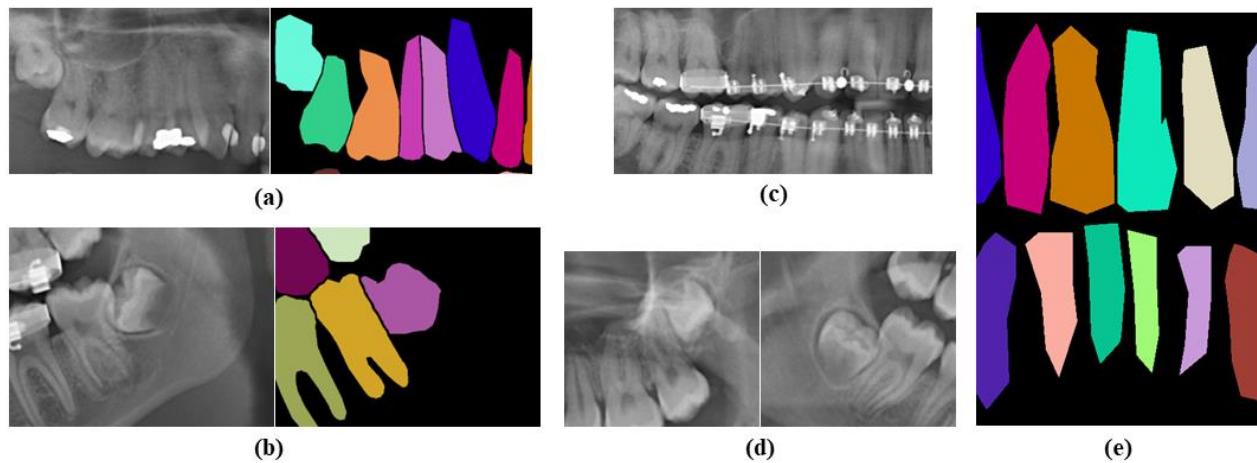


**Figure 9** Problems in the dataset. (a) Overlaps between premolars, and (b) overlaps between premolar and molar. However, in the ground truth there is no instance overlap. (c) Presence of bracelets and fillings, (d) fuzzy molar tooth roots, and (e) poor annotations with sharp edges and cones.

## 5 Conclusion

In this paper, we address the critical tasks of teeth segmentation and orientation in the context of oral healthcare. Accurate teeth segmentation holds immense importance for various applications, including orthodontic treatments, clinical diagnoses, surgical procedures, and dental implant planning. We recognize the challenges posed by manual segmentation, especially in lower-resolution images, and the limitations of existing semi-automatic techniques that still require human intervention. Our model architecture includes an EfficientNet-based encoder and a decoder with grid-based attention gates and a parallel spatial and channel squeeze-and-excitation (P-scSE) module. We also introduce oriented bounding boxes (OBB) generation using principal component analysis (PCA). Our model’s accuracy and capabilities open up new possibilities for improving dental diagnoses and treatment planning. Future works include extending our approach to 3D instance segmentation of teeth, which is crucial for applications like orthognathic surgery planning and dental implant placement, which would be a valuable direction.

## REFERENCE

- [1] A. Polizzi *et al.*, “Tooth automatic segmentation from CBCT images: A systematic review,” *Clinical Oral Investigations*, vol. 27, no. 7, pp. 3363–3378, 2023.
- [2] D. Luo, W. Zeng, J. Chen, and W. Tang, “Deep learning for automatic image segmentation in stomatology and its clinical application,” *Frontiers in Medical Technology*, vol. 3, 2021.
- [3] Y. Huang *et al.*, “Tooth position determination by automatic cutting and marking of dental panoramic X-ray film in medical image processing,” *Applied Sciences*, vol. 11, no. 24, p. 11904, 2021.
- [4] M. K. Dhar, Taiyu Zhang, Yash Patel, and Zeyun Yu., “FUSeNet: A Deep Convolutional Neural Network for Foot Ulcer Segmentation,” *arXiv preprint*, arXiv:2305.02961 (2023).
- [5] B. Silva, L. Pinheiro, L. Oliveira, and M. Pithon, “A study on tooth segmentation and numbering using end-to-end deep neural networks,” *2020 33rd SIBGRAPI Conference on Graphics, Patterns and Images (SIBGRAPI)*, 2020.
- [6] T. L. Koch, M. Perslev, C. Igel, and S. S. Brandt, “Accurate segmentation of dental panoramic radiographs with U-NETS,” *2019 IEEE 16th International Symposium on Biomedical Imaging (ISBI 2019)*, 2019.
- [7] Y. Zhao *et al.*, “TSASNet: Tooth segmentation on dental panoramic x-ray images by two-stage attention segmentation network,” *Knowledge-Based Systems*, vol. 206, p. 106338, 2020.

- [8] Q. Chen *et al.*, “MSLPNet: Multi-scale Location Perception Network for dental panoramic X-ray image segmentation,” *Neural Computing and Applications*, vol. 33, no. 16, pp. 10277–10291, 2021.
- [9] O. Salih and K. J. Duffy, “The local ternary pattern encoder–decoder neural network for dental image segmentation,” *IET Image Processing*, vol. 16, no. 6, pp. 1520–1530, 2022. doi:10.1049/ipr2.12416
- [10] S. Hou *et al.*, “Teeth U-net: A segmentation model of dental panoramic X-ray images for context semantics and contrast enhancement,” *Computers in Biology and Medicine*, vol. 152, p. 106296, 2023.
- [11] G. Jader *et al.*, “Deep instance segmentation of teeth in panoramic X-ray images,” *2018 31st SIBGRAPI Conference on Graphics, Patterns and Images (SIBGRAPI)*, 2018.
- [12] G. Rubiu *et al.*, “Teeth segmentation in panoramic dental x-ray using mask regional convolutional Neural Network,” *Applied Sciences*, vol. 13, no. 13, p. 7947, 2023.
- [13] K. Panetta, R. Rajendran, A. Ramesh, S. Rao, and S. Agaian, “Tufts Dental Database: A multimodal panoramic X-ray dataset for Benchmarking Diagnostic Systems,” *IEEE Journal of Biomedical and Health Informatics*, vol. 26, no. 4, pp. 1650–1659, 2022.
- [14] S. HELLİ and A. HAMAMCI, “Tooth instance segmentation on panoramic dental radiographs using u-nets and morphological processing,” *Düzce Üniversitesi Bilim ve Teknoloji Dergisi*, vol. 10, no. 1, pp. 39–50, 2022.
- [15] A. R. El Bsar *et al.*, “Semantic segmentation of maxillary teeth and palatal rugae in two-dimensional images,” *Diagnostics*, vol. 12, no. 9, p. 2176, 2022.
- [16] M. Turk and A. Pentland, “Eigenfaces for recognition,” *Journal of Cognitive Neuroscience*, vol. 3, no. 1, pp. 71–86, 1991.
- [17] M. Tan and Q. V. Le, “EfficientNet: Rethinking model scaling for convolutional neural networks,” in *Proceedings of the 36th International Conference on Machine Learning (ICML)*, vol. 2019-June, pp. 10691–10700, 2019.
- [18] O. Oktay *et al.*, “Attention U-Net: Learning where to look for the pancreas,” *arXiv preprint*, arXiv:1804.03999, 2018.
- [19] J. Hu, L. Shen, and G. Sun, “Squeeze-and-excitation networks,” *2018 IEEE/CVF Conference on Computer Vision and Pattern Recognition*, 2018.
- [20] A. G. Roy, N. Navab, and C. Wachinger, “Recalibrating fully convolutional networks with spatial and channel ‘squeeze and excitation’ blocks,” *IEEE Transactions on Medical Imaging*, vol. 38, no. 2, pp. 540–549, 2019.
- [21] D. P. Kingma and J. Ba, “Adam: A method for stochastic optimization,” *arXiv preprint*, arXiv:1412.6980, 2014.
- [22] T.-Y. Lin, P. Goyal, R. Girshick, K. He, and P. Dollar, “Focal loss for dense object detection,” *IEEE Transactions on Pattern Analysis and Machine Intelligence*, vol. 42, no. 2, pp. 318–327, 2020.
- [23] M. Kanwal, M. M. Ur Rehman, M. U. Farooq, and D.-K. Chae, “Mask-transformer-based networks for teeth segmentation in panoramic radiographs,” *Bioengineering*, vol. 10, no. 7, p. 843, 2023.
- [24] A. Almalki and L. J. Latecki, “Self-supervised learning with masked image modeling for teeth numbering, detection of dental restorations, and instance segmentation in dental panoramic radiographs,” *2023 IEEE/CVF Winter Conference on Applications of Computer Vision (WACV)*, 2023.
- [25] L.-C. Chen, Y. Zhu, G. Papandreou, F. Schroff, and H. Adam, “Encoder-decoder with atrous separable convolution for Semantic Image segmentation,” *Computer Vision – ECCV 2018*, pp. 833–851, 2018.
- [26] T.-Y. Lin *et al.*, “Feature Pyramid Networks for Object Detection,” *2017 IEEE Conference on Computer Vision and Pattern Recognition (CVPR)*, 2017.
- [27] T. Fan, G. Wang, Y. Li, and H. Wang, “Ma-net: A multi-scale attention network for liver and tumor segmentation,” *IEEE Access*, vol. 8, pp. 179656–179665, 2020.
- [28] A. Chaurasia and E. Culurciello, “LinkNet: Exploiting encoder representations for efficient semantic segmentation,” *2017 IEEE Visual Communications and Image Processing (VCIP)*, 2017.
- [29] H. Zhao, J. Shi, X. Qi, X. Wang, and J. Jia, “Pyramid Scene Parsing Network,” *2017 IEEE Conference on Computer Vision and Pattern Recognition (CVPR)*, 2017.
- [30] O. Ronneberger, P. Fischer, and T. Brox, “U-net: Convolutional networks for biomedical image segmentation,” *Medical Image Computing and Computer-Assisted Intervention – MICCAI 2015: 18th International Conference, Munich, Germany*, pp. 234–241, 2015.
- [31] M. K. Dhar and Mou Deb., “S-R2F2U-Net: A single-stage model for teeth segmentation,” *arXiv preprint*, arXiv: 2204.02939, 2022.
- [32] E. Xie, *et al.*, “SegFormer: Simple and efficient design for semantic segmentation with transformers,” *Advances in Neural Information Processing Systems*, vol. 34, pp. 12077–12090, 2021.
- [33] H. Cao, *et al.* “Swin-unet: Unet-like pure transformer for medical image segmentation,” *European conference on computer vision*. Cham: Springer Nature Switzerland, 2022.
- [34] T. Lin, Y. Wang, X. Liu, and X. Qiu, “A survey of Transformers,” *AI Open*, vol. 3, pp. 111–132, 2022.
- [35] Y. Liu, *et al.*, “Efficient training of visual transformers with small datasets,” in *Proceedings of Advances in Neural Information Processing Systems (NeurIPS)*, vol. 34, pp. 23818–23830, 2021.